

Saturation in Snapshot Compressive Imaging

Mengyu Zhao*, Shirin Jalali*

Abstract

Snapshot Compressive Imaging (SCI) maps three-dimensional (3D) data cubes, such as videos or hyperspectral images, into two-dimensional (2D) measurements via optical modulation, enabling efficient data acquisition and reconstruction. Recent advances have shown the potential of mask optimization to enhance SCI performance, but most studies overlook nonlinear distortions caused by saturation in practical systems. Saturation occurs when high-intensity measurements exceed the sensor’s dynamic range, leading to information loss that standard reconstruction algorithms cannot fully recover. This paper addresses the challenge of optimizing binary masks in SCI under saturation. We theoretically characterize the performance of compression-based SCI recovery in the presence of saturation and leverage these insights to optimize masks for such conditions. Our analysis reveals trade-offs between mask statistics and reconstruction quality in saturated systems. Experimental results using a Plug-and-Play (PnP) style network validate the theory, demonstrating improved recovery performance and robustness to saturation with our optimized binary masks.

1 Introduction

1.1 Snapshot compressive imaging

Snapshot Compressive Imaging (SCI) compresses a three-dimensional (3D) data cube into a two-dimensional (2D) measurement matrix via optical modulation, enabling rapid data acquisition and computationally efficient reconstruction. Initially developed for spectral imaging [1, 2], SCI has revolutionized imaging by eliminating the need for time-intensive scanning across spatial or wavelength domains. For instance, hyperspectral SCI systems capture information across multiple wavelengths in a single snapshot, significantly accelerating the imaging process compared to traditional methods.

Over the years, SCI has been extended to applications such as video [3] and digital holography [4], with increasing attention being given to the optimization of its core component: the optical mask. Masks play a critical role in the encoding process, and their optimization has been shown to considerably improve reconstruction performance. Recent works [5, 6, 7, 8] explore both theoretical and empirical strategies for mask optimization, ranging from theoretically optimizing structured masks to employing end-to-end learning frameworks. However, these studies predominantly assume idealized measurement systems, often neglecting practical limitations such as saturation.

Saturation, a nonlinear distortion that occurs when high-intensity measurements exceed the sensor’s dynamic range, is a significant challenge in imaging applications, including but not limited to SCI. It leads to clipped measurements and information loss that conventional reconstruction algorithms cannot fully recover. Addressing this problem requires tailored mask designs and reconstruction techniques capable of mitigating saturation’s impact. This raises two central questions for this work:

1. Can we theoretically characterize the performance of SCI recovery under saturated measurements?

*Rutgers University, New Brunswick, Department of Electrical and Computer Engineering (mengyu.zhao@rutgers.edu, shirin.jalali@rutgers.edu).

2. What strategies can optimize binary masks to improve recovery performance in the presence of saturation?

In this paper, we address these questions by developing a theoretical framework for analyzing compression-based SCI recovery under saturation conditions. We then propose an optimization approach for binary masks, demonstrating its effectiveness through both theoretical insights and empirical validation. While our focus is on SCI, the insights and methodologies developed in this work have the potential to inform future efforts in addressing saturation challenges in other computational imaging applications.

1.2 Mathematical model

Mathematically, an SCI system can be described as follows. Let $\mathbf{X} \in \mathbb{R}^{n_1 \times n_2 \times B}$ represent the desired 3D data cube. An SCI system transforms \mathbf{X} into a single measurement frame $\mathbf{Y} \in \mathbb{R}^{n_1 \times n_2}$. In various SCI systems, including hyperspectral (HS) SCI [1] and video SCI [3], the transformation from \mathbf{X} to \mathbf{Y} can be represented by a linear model such that [3, 9],

$$\mathbf{Y} = \sum_{b=1}^B \mathbf{C}_b \odot \mathbf{X}_b + \mathbf{Z}.$$

Here, $\mathbf{C} \in \mathbb{R}^{n_1 \times n_2 \times B}$ and $\mathbf{Z} \in \mathbb{R}^{n_1 \times n_2}$ correspond to the sensing kernel (mask) and additive noise, respectively. Specifically, $\mathbf{C}_b = \mathbf{C}(:, :, b)$ and $\mathbf{X}_b = \mathbf{X}(:, :, b) \in \mathbb{R}^{n_1 \times n_2}$ denote the b -th sensing kernel (mask) and the associated signal frame, respectively; \odot refers to the Hadamard (element-wise) product.

To simplify the mathematical representation of the system, each frame is vectorized as $\mathbf{x}_b = \text{Vec}(\mathbf{X}_b) \in \mathbb{R}^n$, where $n = n_1 n_2$. The data cube \mathbf{X} is then vectorized by concatenating the B vectorized frames into a single column vector $\mathbf{x} \in \mathbb{R}^{nB}$, expressed as

$$\mathbf{x} = \left[\mathbf{x}_1^\top, \dots, \mathbf{x}_B^\top \right]^\top. \quad (1)$$

Similarly, we define $\mathbf{y} = \text{Vec}(\mathbf{Y}) \in \mathbb{R}^n$ and $\mathbf{z} = \text{Vec}(\mathbf{Z}) \in \mathbb{R}^n$. Using these definitions, the measurement process can be described as

$$\mathbf{y} = \mathbf{H}\mathbf{x} + \mathbf{z}, \quad (2)$$

where the sensing matrix $\mathbf{H} \in \mathbb{R}^{n \times nB}$ is a highly sparse matrix constructed by concatenating B diagonal matrices as

$$\mathbf{H} = [\mathbf{D}_1, \dots, \mathbf{D}_B], \quad (3)$$

with $\mathbf{D}_b = \text{diag}(\text{Vec}(\mathbf{C}_b)) \in \mathbb{R}^{n \times n}$ for $b = 1, \dots, B$.

The goal of an SCI recovery algorithm is to reconstruct the data cube $\mathbf{x} \in \mathbb{R}^{nB}$ from the undersampled measurements $\mathbf{y} \in \mathbb{R}^n$, given access to the sensing matrix (or mask) \mathbf{H} .

1.3 Compression-based SCI

An important challenge in analyzing SCI systems lies in modeling the structure of 3D data cubes, such as videos or hyperspectral (HS) images. A prominent approach to address this is compression-based recovery, initially introduced in the context of compressed sensing [10]. This technique utilizes compression codes to implicitly capture the structure of signal classes, enabling more efficient representation. The fundamental idea involves leveraging these codes to solve inverse problems, where the compression code serves as a black-box model for the signal structure. This approach was later extended to SCI systems in [11], providing the first theoretical analysis in this domain.

Consider a class of signals representing B -frame data cubes of a certain type, e.g., video or hyperspectral images. This class of signals is represented by a compact set \mathcal{Q} , $\mathcal{Q} \subset \mathbb{R}^{nB}$. A rate- r compression code for

\mathcal{Q} is characterized by an encoder-decoder pair (f, g) , where $f : \mathbb{R}^{nB} \rightarrow 1, \dots, 2^{Br}$ and $g : 1, \dots, 2^{Br} \rightarrow \mathbb{R}^{nB}$. For $\mathbf{x} \in \mathcal{Q}$, the reconstructed signal $\tilde{\mathbf{x}}$ is obtained as $\tilde{\mathbf{x}} = g(f(\mathbf{x}))$, with distortion measured as

$$d_{nB}(\mathbf{x}, \tilde{\mathbf{x}}) = \frac{1}{nB} \|\mathbf{x} - \tilde{\mathbf{x}}\|_2^2.$$

The codebook corresponding to this code is defined as $\mathcal{C} = g(f(\mathbf{x})) : \mathbf{x} \in \mathcal{Q}$. By design, $|\mathcal{C}| \leq 2^{Br}$. The distortion of the code is then defined as:

$$\delta = \sup_{\mathbf{x} \in \mathcal{Q}} d_{nB}(\mathbf{x}, g(f(\mathbf{x}))).$$

In SCI recovery, the goal is to reconstruct \mathbf{x} from underdetermined measurements \mathbf{y} . Compression-based recovery bypasses explicit structural modeling by capturing the structure through a compression code. Given a compression code (f, g) operating at rate r and distortion δ , the compression-based SCI recovery problem is expressed as:

$$\hat{\mathbf{x}} = \arg \min_{\mathbf{c} \in \mathcal{C}} \|\mathbf{y} - \sum_{i=1}^B \mathbf{D}_i \mathbf{c}_i\|_2^2. \quad (4)$$

Previous theoretical studies [11, 7, 8, 12] have analyzed this approach for both Gaussian and various types of binary diagonal matrices \mathbf{D}_i , as well as in the presence of white noise corruption on the measurements. This paper builds on these results by extending the analysis to practical SCI system masks operating under saturated conditions.

1.4 Notations

Vectors are represented using bold characters, such as \mathbf{x} and \mathbf{y} . For a matrix $\mathbf{X} \in \mathbb{R}^{n_1 \times n_2}$, $\text{Vec}(\mathbf{X}) \in \mathbb{R}^n$ represents its vectorized form, where $n = n_1 n_2$. This vector is constructed by concatenating the columns of \mathbf{X} . For $\mathbf{A}, \mathbf{B} \in \mathbb{R}^{n_1 \times n_2}$, the Hadamard product $\mathbf{Y} = \mathbf{A} \odot \mathbf{B}$ is defined element-wise such that $Y_{ij} = A_{ij} B_{ij}$ for all i, j . Sets are denoted by calligraphic letters, such as \mathcal{A} and \mathcal{B} . For a finite set \mathcal{A} , $|\mathcal{A}|$ indicates the number of elements in \mathcal{A} .

2 Related work

The saturation effect can severely degrade the performance of any imaging system. Previous theoretical analyses of saturation have primarily been conducted within the general compressed sensing framework in signal processing. [13] addressed saturation in CS systems with algorithms like saturation rejection and saturation consistency. In [14] and [15], the authors handle presaturation errors and Gaussian noise, with proven performance bounds. An open question remains: can saturation in SCI be effectively addressed through theoretical and algorithmic solutions? Despite the significance of this issue, few studies have explored it, with most approaching the problem from an optical science perspective. Among these works, some focus on designing structural masks (coded apertures) specifically to handle corrupted scenarios. To achieve full dynamic range in video SCI, [16] proposed an end-to-end network trained simultaneously on reconstruction and a trainable mask. Their findings demonstrated that masks following specific distributions yield better results. In [17, 18], they add a preprocessed step with point spread function (PSF) before capture the original video to to encode more details followed by reconstruction with deep optics. In [19], authors proposed a learnable sensor in the measuring pipeline jointed optimized the process. With the learned optical coding would generate favorable results. In the context of general corrupted measurement processes, [8, 7] provided both theoretical and algorithmic evidence demonstrating that optimizing mask distributions can be beneficial. For hyperspectral SCI, [20] introduced blue noise to the coded aperture to mitigate saturation effects. Additionally, [21] designed a real-time updating grayscale coded aperture system to reduce laser interference by lowering the power density on the measurement, thereby avoiding sensor saturation.

3 SCI under measurement saturation

3.1 Mathematical model

We model the impact of saturation on SCI measurements using a non-linear function $f_T : \mathbb{R}^+ \rightarrow \mathbb{R}^+$, defined as follows. Let $T \in \mathbb{R}^+$ represent the threshold level for saturation, and let $y \in \mathbb{R}^+$.

$$f(y) = \begin{cases} y, & \text{if } y < T, \\ T, & \text{if } y \geq T. \end{cases}$$

Given an SCI system characterized by masks $[\mathbf{D}_1, \dots, \mathbf{D}_B]$, the saturated measurements are defined as

$$\mathbf{y}_T = f_T(\mathbf{y}),$$

where $\mathbf{y} = \sum_{i=1}^B \mathbf{D}_i \mathbf{x}_i$ and $f_T(\cdot)$ is applied element-wise to all entries of \mathbf{y} such that $y_{T,i} = f_T(y_i)$. Note that when the masks are binary-valued and all $\mathbf{x} \in \mathcal{Q}$ satisfy $\|\mathbf{x}\|_\infty \leq \frac{\rho}{2}$,

$$|y_i| = \left| \sum_{i=1}^B D_{ij} x_{ij} \right| \leq \frac{B\rho}{2}.$$

Therefore, choosing $\mathbf{y}_T = T \geq B\rho/2$, leads to the identity function and $f_T(\mathbf{y}) = \mathbf{y}$.

3.2 Main theoretical results

Define the set \mathcal{I}_s to represent the indices where the measurements are saturated, such that:

$$\mathcal{I}_s = \left\{ j : \sum_{i=1}^B D_{ij} x_{ij} \geq T \right\}.$$

The performance of SCI recovery under saturation depends critically on the number of saturated elements (or pixels), denoted by $|\mathcal{I}_s|$. For a given $\mathbf{x} \in \mathbb{R}^{nB}$, $T > 0$, and $\epsilon > 0$, we define:

$$p_s(\mathbf{x}; T) \triangleq \frac{1}{n} \mathbb{E}[|\mathcal{I}_s|],$$

and

$$E_s(\mathbf{x}; T, \epsilon) \triangleq \mathbb{P}(|\mathcal{I}_s| \geq \mathbb{E}[|\mathcal{I}_s|] + n\epsilon),$$

where $p_s(\mathbf{x}; T)$ denotes the expected fraction of saturated measurements, and $E_s(\mathbf{x}; T, \epsilon)$ characterizes the probability of significant deviation of $|\mathcal{I}_s|$ from its expected value. Using these definitions, the following theorem quantifies the impact of measurement saturation on compression-based SCI recovery.

Theorem 3.1. *Consider $\mathcal{Q} \subset \mathbb{R}^{nB}$, where for all $\mathbf{x} \in \mathcal{Q}$, $\|\mathbf{x}\|_\infty \leq \frac{\rho}{2}$. Let \mathcal{C} denote the codebook corresponding to a rate- r distortion- δ lossy compression code for signals in \mathcal{Q} . Assume that $\mathbf{D}_1 \dots \mathbf{D}_B$ are such that $\mathbf{D}_i = \text{diag}(D_{i1} \dots D_{in})$, $i = 1, \dots, B$, where the diagonal entries of the matrices drawn independently i.i.d. Bern(p). For $\mathbf{x} \in \mathcal{Q}$ and $\mathbf{y} = \sum_{i=1}^B \mathbf{D}_i \mathbf{x}_i$, let $\hat{\mathbf{x}}$ denote the solution of (4). Choose the free parameters $\epsilon_1, \epsilon_2 > 0$. Then, Assume that $\mathbf{y} = f_T(\sum_{i=1}^B \mathbf{D}_i \mathbf{x}_i)$.*

$$\begin{aligned} \frac{1}{nB} \|\mathbf{x} - \hat{\mathbf{x}}\|^2 &\leq \left(1 + \frac{Bp}{1-p}\right)\delta + \frac{\rho^2 \epsilon_1}{p(1-p)} \\ &+ \frac{1}{B} (p_s(\mathbf{x}; T) + \epsilon_2) \left(\frac{B\rho}{2} - T\right)^+ \left(\left(\frac{B\rho}{2} - T\right)^+ + 4B\rho\right) \end{aligned} \quad (5)$$

with probability larger than $1 - 2^{Br+1} \exp\left(-\frac{n\epsilon_1^2}{2B^2}\right) - E_s(\mathbf{x}; T, \epsilon_2)$.

If $p_s(\mathbf{x}; T) = 0$, the result of Theorem 3.1 reduces to the ideal case, where no measurements are saturated, as detailed in Theorem 1 in [7]. The second term quantifies the increase in reconstruction error caused by saturation. Notably, increasing the threshold T reduces this term, as both $p_s(\mathbf{x}; T)$ and $(\frac{B\rho}{2} - T)^+((\frac{B\rho}{2} - T)^+ 4B\rho)$ are decreasing functions of T . At $T = \frac{B\rho}{2}$, the additional error term becomes zero.

The following corollary of Theorem 3.1, addresses Question 2 mentioned earlier. That is, the effect of measurements saturation on the optimal mask distribution. For a given $T > 0$, let p_T^* denote the minimizer of the bound in Theorem 3.1. In other words, for a given T , generating the elements of the masks according to $\text{Bern}(p_T^*)$ leads to the minimum recovery error bound.

Corollary 3.2. *For any $T > 0$, $p_T^* < \frac{1}{2}$. Furthermore, p_T^* is a decreasing function of T .*

To further understand Theorem 3.1 and the effect of the threshold T on performance, one needs to analyze $p_s(\mathbf{x}; T)$ and $E_s(\mathbf{x}; T, \epsilon)$. However, directly modeling the statistical behavior of the 3D data (e.g., video) is challenging. Therefore, we make reasonable simplifying assumptions to gain insight.

The number of saturated elements can be expressed as:

$$|\mathcal{I}_s| = \sum_{j=1}^n \mathbb{1}_{\sum_{i=1}^B D_{ij} x_{ij} \geq T}.$$

Given $\mathbf{u} \in (\mathbb{R}^+)^B$, define

$$\eta(T; \mathbf{u}) \triangleq \text{P}\left(\sum_{i=1}^B D_{ij} u_i > T\right),$$

where D_{1j}, \dots, D_{Bj} are i.i.d. $\text{Bern}(p)$. Clearly $\eta(0; \mathbf{u}) = 1$ and $\lim_{T \rightarrow \infty} \eta(T; \mathbf{u}) = 0$. Moreover,

$$\text{E}[|\mathcal{I}_s|] = np_s(\mathbf{x}; T) = \sum_{j=1}^n \eta(T; (x_{1j}, \dots, x_{Bj})). \quad (6)$$

Let

$$\bar{\mathbf{x}} = \frac{1}{B} \sum_{i=1}^B \mathbf{x}_i.$$

Then,

$$\mathbf{y} = \sum_{i=1}^B \mathbf{D}_i \mathbf{x}_i = \bar{\mathbf{x}} \sum_{i=1}^B \mathbf{D}_i + \sum_{i=1}^B \mathbf{D}_i (\mathbf{x}_i - \bar{\mathbf{x}})$$

The measurements thus decompose into two components: one coming from the mean of the frames, and the other resulting from the effect of the deviations of the frames from their mean. Note that in SCI applications, the frames are highly correlated, making it reasonable to assume that the deviations $\mathbf{x}_i - \bar{\mathbf{x}}$ are small compared to the mean $\bar{\mathbf{x}}$. For high-level insights, we focus on the primary component and make the following approximation

$$\sum_{i=1}^B \mathbf{D}_i \mathbf{x}_i \approx \bar{\mathbf{x}} \sum_{i=1}^B \mathbf{D}_i.$$

Given $x \in \mathbb{R}^+$, define

$$\bar{\eta}(T; \bar{x}) = \text{P}\left(\bar{x} \sum_{i=1}^B D_{ij} > T\right) = \eta(T; \underbrace{\bar{x}(1, \dots, 1)}_B)$$

Then, using this simplification enables us to approximate the desired probability as

$$\begin{aligned}
E_s(\mathbf{x}; T, \epsilon) &= \mathbb{P}(|\mathcal{I}_s| \geq \mathbb{E}[|\mathcal{I}_s|] + n\epsilon) \\
&= \mathbb{P}\left(\sum_{j=1}^n (\mathbb{1}_{\sum_{i=1}^B D_{ij} x_{ij} \geq T} - \eta(T; (x_{1j}, \dots, x_{Bj}))) \geq n\epsilon\right) \\
&\approx \mathbb{P}\left(\sum_{j=1}^n (\mathbb{1}_{\bar{x}_i \sum_{i=1}^B D_{ij} \geq T} - \bar{\eta}(T; \bar{x}_j)) \geq n\epsilon\right) \\
&= \mathbb{P}\left(\frac{1}{n} \sum_{j=1}^n \mathbb{1}_{\bar{x}_i \sum_{i=1}^B D_{ij} \geq T} - \mathbb{E}_J[\bar{\eta}(T; \bar{x}_J)] \geq n\epsilon\right), \tag{7}
\end{aligned}$$

where J is independently distributed over $\{1, \dots, n\}$, such that $\mathbb{P}(J = j) = \frac{1}{n}$. That is,

$$\mathbb{E}_J[\bar{\eta}(T; \bar{x}_J)] = \frac{1}{n} \sum_{j=1}^n \bar{\eta}(T; \bar{x}_j)$$

On the other hand, using the Hoeffding's inequality, we have

$$\mathbb{P}\left(\frac{1}{n} \sum_{j=1}^n \mathbb{1}_{\bar{x}_i \sum_{i=1}^B D_{ij} \geq T} - \mathbb{E}_J[\bar{\eta}(T; \bar{x}_J)] \geq n\epsilon\right) \leq e^{-n\epsilon^2/2}. \tag{8}$$

Therefore, combing (7) and (8), we have

$$\begin{aligned}
&\mathbb{P}(|\mathcal{I}_s| \geq \mathbb{E}[|\mathcal{I}_s|] + n\epsilon) \\
&\approx \mathbb{P}\left(\frac{1}{n} \sum_{j=1}^n \mathbb{1}_{\bar{x}_i \sum_{i=1}^B D_{ij} \geq T} - \mathbb{E}[\bar{\eta}(T; \bar{x}_J)] \geq n\epsilon\right) \\
&\leq e^{-n\epsilon^2/2}. \tag{9}
\end{aligned}$$

Moreover, using the same approximation,

$$p_s(\mathbf{x}; T) \approx \mathbb{E}_J[\bar{\eta}(T; \bar{x}_J)].$$

Finally, the following lemma provides a simple upper bound on $\mathbb{E}_J[\bar{\eta}(T; \bar{x}_J)]$.

Lemma 3.1. *For any $\mathbf{x} \in \mathbb{R}^{nB}$,*

$$\mathbb{E}_J[\bar{\eta}(T; \bar{x}_J)] \leq \frac{1}{n} \|\bar{\mathbf{x}}\|_2^2 \frac{Bp(1 + (B-1)p)}{T^2}. \tag{10}$$

4 Proofs

This section contains the proofs of the results stated earlier in the paper.

4.1 Proof for Theorem 3.1

Let $\tilde{\mathbf{x}} = g(f(\mathbf{x}))$. By assumption, since $\mathbf{x} \in \mathcal{Q}$, $\|\mathbf{x} - \tilde{\mathbf{x}}\|_2^2 \leq nB\delta$. Let

$$\mathbf{y} = f_T\left(\sum_{i=1}^B \mathbf{D}_i \mathbf{x}_i\right), \quad \text{and} \quad \mathbf{y}^{\text{ideal}} = \sum_{i=1}^B \mathbf{D}_i \mathbf{x}_i,$$

denote the measurement vector and the ideal measurement vector, respectively. Since $\hat{\mathbf{x}} = \arg \min_{\mathbf{c} \in \mathcal{C}} \|\mathbf{y} - \sum_{i=1}^B \mathbf{D}_i \mathbf{c}_i\|_2^2$, and $\tilde{\mathbf{x}} \in \mathcal{C}$, it follows that

$$\|f_T(\sum_{i=1}^B \mathbf{D}_i \mathbf{x}_i) - \sum_{i=1}^B \mathbf{D}_i \hat{\mathbf{x}}_i\|_2 \leq \|f_T(\sum_{i=1}^B \mathbf{D}_i \mathbf{x}_i) - \sum_{i=1}^B \mathbf{D}_i \tilde{\mathbf{x}}_i\|_2. \quad (11)$$

Therefore,

$$\begin{aligned} & \sum_{j \in \mathcal{I}_s} (T - \sum_{i=1}^B D_{ij} \hat{x}_{ij})^2 + \sum_{j \in \mathcal{I}_s^c} (\sum_{i=1}^B D_{ij} (x_{ij} - \hat{x}_{ij}))^2 \\ & \leq \sum_{j \in \mathcal{I}_s} (T - \sum_{i=1}^B D_{ij} \tilde{x}_{ij})^2 + \sum_{j \in \mathcal{I}_s^c} (\sum_{i=1}^B D_{ij} (x_{ij} - \tilde{x}_{ij}))^2 \end{aligned} \quad (12)$$

Let $U = \sum_{j \in \mathcal{I}_s} (T - \sum_{i=1}^B D_{ij} \tilde{x}_{ij})^2 + \sum_{j \in \mathcal{I}_s^c} (\sum_{i=1}^B D_{ij} (x_{ij} - \tilde{x}_{ij}))^2$. Then,

$$\begin{aligned} U &= \sum_{j \in \mathcal{I}_s} (y_j - y_j^{\text{ideal}} + y_j^{\text{ideal}} - \sum_{i=1}^B D_{ij} \tilde{x}_{ij})^2 + \sum_{j \in \mathcal{I}_s^c} (\sum_{i=1}^B D_{ij} (x_{ij} - \tilde{x}_{ij}))^2 \\ &\stackrel{(a)}{\leq} |\mathcal{I}_s| \left(\frac{B\rho}{2} - T\right)^2 + 2 \sum_{j \in \mathcal{I}_s} (y_j - y_j^{\text{ideal}}) (y_j^{\text{ideal}} - \sum_{i=1}^B D_{ij} \tilde{x}_{ij}) \\ &\quad + \sum_{j \in \mathcal{I}_s} (\sum_{i=1}^B D_{ij} (x_{ij} - \tilde{x}_{ij}))^2 + \sum_{j \in \mathcal{I}_s^c} (\sum_{i=1}^B D_{ij} (x_{ij} - \tilde{x}_{ij}))^2 \\ &\leq |\mathcal{I}_s| \left(\frac{B\rho}{2} - T\right)^2 + 2 \sum_{j \in \mathcal{I}_s} |y_j - y_j^{\text{ideal}}| |y_j^{\text{ideal}} - \sum_{i=1}^B D_{ij} \tilde{x}_{ij}| + \left\| \sum_{i=1}^B \mathbf{D}_i (\mathbf{x}_i - \tilde{\mathbf{x}}_i) \right\|^2 \\ &\stackrel{(b)}{\leq} |\mathcal{I}_s| \left(\frac{B\rho}{2} - T\right)^+ \left(\left(\frac{B\rho}{2} - T\right)^+ + 2B\rho \right) + \left\| \sum_{i=1}^B \mathbf{D}_i (\mathbf{x}_i - \tilde{\mathbf{x}}_i) \right\|^2, \end{aligned} \quad (13)$$

where (a) and (b) follow because for $j \in \mathcal{I}_s$, $|y_j - y_j^{\text{ideal}}| \leq (\frac{B\rho}{2} - T)^+$ and $|y_j^{\text{ideal}} - \sum_{i=1}^B D_{ij} \tilde{x}_{ij}| \leq B\rho$, respectively.

Similarly, let $L = \sum_{j \in \mathcal{I}_s} (T - \sum_{i=1}^B D_{ij} \hat{x}_{ij})^2 + \sum_{j \in \mathcal{I}_s^c} (\sum_{i=1}^B D_{ij} (x_{ij} - \hat{x}_{ij}))^2$. Then,

$$\begin{aligned} L &= \sum_{j \in \mathcal{I}_s} (y_j^s - y_j + y_j - \sum_{i=1}^B D_{ij} \hat{x}_{ij})^2 + \sum_{j \in \mathcal{I}_s^c} (\sum_{i=1}^B D_{ij} (x_{ij} - \hat{x}_{ij}))^2 \\ &\geq -2 \sum_{j \in \mathcal{I}_s} |y_j^s - y_j| |y_j - \sum_{i=1}^B D_{ij} \hat{x}_{ij}| + \left\| \sum_{i=1}^B \mathbf{D}_i (\mathbf{x}_i - \hat{\mathbf{x}}_i) \right\|^2 \\ &\geq -2|\mathcal{I}_s| \left(\frac{B\rho}{2} - T\right)^+ B\rho + \left\| \sum_{i=1}^B \mathbf{D}_i (\mathbf{x}_i - \hat{\mathbf{x}}_i) \right\|^2. \end{aligned} \quad (14)$$

Since from (12), $L \leq U$, combining (13) and (14), it follows that

$$\left\| \sum_{i=1}^B \mathbf{D}_i (\mathbf{x}_i - \hat{\mathbf{x}}_i) \right\|^2 \leq \left\| \sum_{i=1}^B \mathbf{D}_i (\mathbf{x}_i - \tilde{\mathbf{x}}_i) \right\|^2 + |\mathcal{I}_s| \left(\frac{B\rho}{2} - T\right)^+ \left(\left(\frac{B\rho}{2} - T\right)^+ + 4B\rho \right). \quad (15)$$

Given $\epsilon_1 > 0$ and $\epsilon_2 > 0$ define events \mathcal{E}_1 , \mathcal{E}_2 and \mathcal{E}_s as

$$\mathcal{E}_1 = \left\{ \frac{1}{n} \left\| \sum_{i=1}^B \mathbf{D}_i(\mathbf{x}_i - \tilde{\mathbf{x}}_i) \right\|_2^2 \leq \frac{p^2}{n} \left\| \sum_{i=1}^B (\mathbf{x}_i - \tilde{\mathbf{x}}_i) \right\|_2^2 + \frac{p-p^2}{n} \|\mathbf{x} - \tilde{\mathbf{x}}\|_2^2 + B\rho^2\epsilon_1/2 \right\}, \quad (16)$$

$$\mathcal{E}_2 = \left\{ \frac{1}{n} \left\| \sum_{i=1}^B \mathbf{D}_i(\mathbf{x}_i - \mathbf{c}_i) \right\|_2^2 \geq \frac{p^2}{n} \left\| \sum_{i=1}^B (\mathbf{x}_i - \mathbf{c}_i) \right\|_2^2 + \frac{p-p^2}{n} \|\mathbf{x} - \mathbf{c}\|_2^2 - B\rho^2\epsilon_1/2 : \forall \mathbf{c} \in \mathcal{C} \right\}, \quad (17)$$

and $\mathcal{E}_s = \{|\mathcal{I}_s| \leq \mathbb{E}[|\mathcal{I}_s|] + n\epsilon_2\}$. Then, conditioned on $\mathcal{E}_1 \cap \mathcal{E}_2 \cap \mathcal{E}_s$, the desired upper bound in (5) follows. Finally, to finish the proof, we need to bound $\mathbb{P}((\mathcal{E}_1 \cap \mathcal{E}_2 \cap \mathcal{E}_s)^c) \leq \mathbb{P}(\mathcal{E}_1^c) + \mathbb{P}(\mathcal{E}_2^c) + \mathbb{P}(\mathcal{E}_s^c)$. By the definition, $\mathbb{P}(\mathcal{E}_s^c) \leq E_s(\mathbf{x}; T, \epsilon_2)$. Using the union bound combined by the Hoeffding's inequality, as done in [7], we have $\mathbb{P}(\mathcal{E}_1^c) + \mathbb{P}(\mathcal{E}_2^c) \leq 2^{Br+1} \exp(-\frac{n\epsilon_1^2}{4B^2})$, which finishes the proof.

4.2 Proof of Corollary 3.2

Let $\delta' = \delta/\rho^2$, $T' = T/\rho$ and $\Delta_T = (\frac{B}{2} - T')^+ \left((\frac{B}{2} - T')^+ + 4B \right)$. Note that Δ_T does not depend on p . The upper bound in Theorem 3.1 normalized by ρ^2 can be written as $g(p)$, where

$$g(p; T) = \left(1 + \frac{Bp}{1-p}\right) \delta' + \frac{\epsilon_1}{p(1-p)} + \frac{1}{B} (p_s(\mathbf{x}; T) + \epsilon_2) \Delta_T. \quad (18)$$

Obviously minimizing $g(p)$ is equivalent to minimizing the bound in Theorem 3.1. Note that

$$g'(p; T) = \frac{B}{(1-p)^2} \delta' + \frac{\epsilon_1(2p-1)}{p^2(1-p)^2} + \frac{\Delta_T}{B} \frac{\partial p_s(\mathbf{x}; T)}{\partial p}. \quad (19)$$

Let p_T^* denote the solution of $g'(p; T)$. Then,

$$\epsilon_1(1-2p_T^*) = B(p_T^*)^2 \delta' + \frac{\Delta_T (p_T^*)^2 (1-p_T^*)^2}{B} \frac{\partial p_s(\mathbf{x}; T)}{\partial p} \Big|_{p=p_T^*}. \quad (20)$$

Recall that $p_s(\mathbf{x}; T)$ denotes the expected number of measurements that are saturated. Therefore, increasing p , which leads to increasing the number of non-zero entries in the masks, only increases $p_s(\mathbf{x}; T)$. Hence, $p_s(\mathbf{x}; T)$ is always an increasing function of p . Hence, from (20),

$$1 - 2p_T^* \geq 0,$$

for all values of T , which implies that $p_T^* \leq \frac{1}{2}$. To finish the proof, we need to show that p_T^* is a decreasing function of T . Consider $T_2 > T_1$ and assume that at T_1 the bound is optimized at $p_{T_1}^*$. That is,

$$\frac{B}{(1-p_{T_1}^*)^2} \delta' + \frac{\epsilon_1(2p_{T_1}^* - 1)}{(p_{T_1}^*)^2(1-p_{T_1}^*)^2} + \frac{\Delta_{T_1}}{B} \frac{\partial p_s(\mathbf{x}; T)}{\partial p} \Big|_{p=p_{T_1}^*} = 0$$

Increasing T from T_1 to T_2 , we need to find the solution of $g'(p; T_2) = 0$. Note that

$$\begin{aligned} g'(p_{T_1}^*; T_2) &= \frac{B}{(1-p_{T_1}^*)^2} \delta' + \frac{\epsilon_1(2p_{T_1}^* - 1)}{(p_{T_1}^*)^2(1-p_{T_1}^*)^2} + \frac{\Delta_{T_2}}{B} \frac{\partial p_s(\mathbf{x}; T)}{\partial p} \Big|_{p=p_{T_1}^*} \\ &= \frac{\Delta_{T_2} - \Delta_{T_1}}{B} \frac{\partial p_s(\mathbf{x}; T)}{\partial p} \Big|_{p=p_{T_1}^*} \end{aligned} \quad (21)$$

But since Δ_T is a decreasing function of T , $\Delta_{T_2} > \Delta_{T_1}$. Hence,

$$g'(p_{T_1}^*; T_2) > 0,$$

which implies that the location where $g'(p; T_2) = 0$ happens at some $p_{T_2}^* < p_{T_1}^*$. In other words, p^* is a decreasing function of T .

4.3 Proof of Lemma 3.1

Using the Chebyshev’s inequality, we have

$$\begin{aligned}
 E_J[\bar{\eta}(T; \bar{x}_J)] &= \frac{1}{n} \sum_{j=1}^n P(\bar{x}_j \sum_{i=1}^B D_{ij} > T) \\
 &\leq \frac{1}{n} \sum_{j=1}^n \frac{E[(\bar{x}_j \sum_{i=1}^B D_{ij})^2]}{T^2} \\
 &\leq \frac{(Bp + B(B-1)p^2)}{T^2 n} \sum_{j=1}^n \bar{x}_j^2,
 \end{aligned} \tag{22}$$

which yields the desired result.

5 Experiments

In the previous sections, we analyzed the performance of compression-based SCI recovery under measurement saturation and examined the effect of mask parameters on recovery performance. In this section, we focus on video SCI, optimizing recovery performance as a function of p under the studied mask models.

Directly solving the optimization problem in (4) is highly challenging, as it requires an exhaustive search over an exponentially large set of codewords. Projected Gradient Descent (PGD) is an efficient algorithm for such problems when the projection set is convex. However, in this case, the set \mathcal{C} is discrete and inherently non-convex. Despite this, in the absence of saturation, it has been shown that PGD can still be effective, converging to the vicinity of the optimal solution [12].

Using PGD to solve (4) becomes even more complex in practice due to the need for heuristic tuning of the compression code parameters (δ, r) as the algorithm progresses. To address these challenges and simplify implementation, we incorporate a robust pretrained denoiser, namely PnP-FastDVDnet [22], which provides enhanced flexibility and adaptability.

The details of our implemented method are outlined in Algorithm 1. In our approach, the gradient descent step is replaced by the Generalized Alternating Projection (GAP) [23] step: $\mathbf{s}^{t+1} = \mathbf{x}^t + \mu \mathbf{H}^\top (\mathbf{H}^\top \mathbf{H})^{-1} \mathbf{e}^t$, where μ is the learning rate. GAP is computationally efficient in SCI applications due to the diagonal structure of the sensing matrices. Compared to gradient descent, GAP eliminates the need for manually tuning the learning rate, a common challenge in traditional approaches. For our implementation, we set the learning rate to $\mu = 1$.

Algorithm 1 PnP-FastDVD framework for SCI recovery

Require: \mathbf{H}, \mathbf{y} .

- 1: Initial $\mu > 0, \mathbf{x}^0 = 0$.
 - 2: **for** $t = 0$ to Max-Iter **do**
 - 3: Calculate: $\mathbf{e}^t = \mathbf{y} - \mathbf{H}\mathbf{x}^t$.
 - 4: GAP step: $\mathbf{s}^{t+1} = \mathbf{x}^t + \mu \mathbf{H}^\top (\mathbf{H}^\top \mathbf{H})^{-1} \mathbf{e}^t$.
 - 5: Projection step via deep denoiser: $\mathbf{x}^{t+1} = \mathcal{D}(\mathbf{s}^{t+1})$.
 - 6: **end for**
 - 7: **Output:** Reconstructed signal $\hat{\mathbf{x}}$.
-

In our implementations we focus on the six benchmark grayscale datasets: **Kobe**, **Runner**, **Drop**, **Traffic**, **Aerial**, and **Vehicle** [22]. Each dataset has a spatial resolution of 256×256 and varying numbers of frames, ranging from 8 to 48.

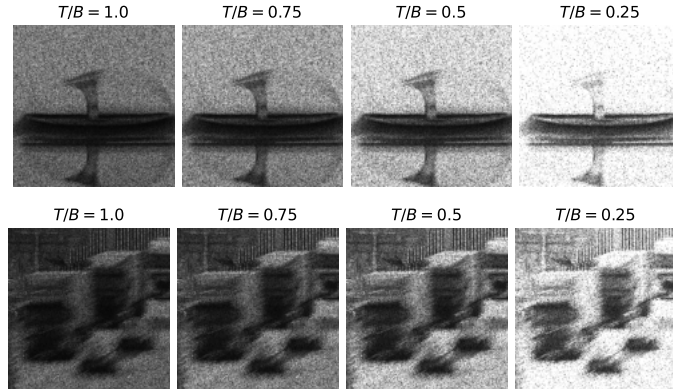


Figure 1: Measurements of **Drop** and **Traffic** modulated with default mask ($\text{Bern}(p = 0.5)$) under different **saturation** level of T .

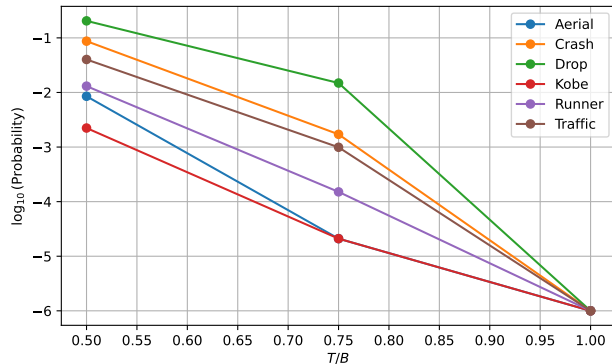


Figure 2: $p_s(\mathbf{x}; T)$, expected fraction of saturated measurements for different input data (\mathbf{x}), as a function of T/B .

5.1 Saturated measurements' distribution

In real-world applications, the saturation threshold is typically fixed. The dynamic parameter that varies during imaging is the illumination of the data. Mathematically, varying the input's illumination with a fixed threshold is equivalent to fixing the input data and adjusting the threshold. Consequently, in both our simulations and theoretical analysis, we keep \mathbf{x} and its illumination fixed while varying the threshold T .

As illustrated in Fig. 1, decreasing the threshold T increases the percentage of saturated measurements, resulting in greater information loss.

Theorem 3.1 characterizes the performance of SCI recovery under measurement saturation. The upper bound in (5) depends on $p_s(\mathbf{x}; T)$, which represents the expected fraction of measurements that are saturated. The value of $p_s(\mathbf{x}; T)$ depends on the properties of \mathbf{x} . To provide further insight into this quantity and its dependence on the input data, Fig. 2 presents $p_s(\mathbf{x}; T)$ for six different inputs.

The figure reveals significant variations in the behavior of $p_s(\mathbf{x}; T)$ across different inputs. For instance, the **Drop** and **Crash** datasets exhibit approximately 10% saturated measurements when $T = 4$, which substantially impacts the recovery performance. In contrast, the **Kobe** dataset has orders of magnitude fewer saturated measurements under the same threshold.

In both figures, the elements of the masks are drawn i.i.d. $\text{Bern}(0.5)$. In the next section, we explore the impact of the masks’ distribution on the performance.

5.2 SCI recovery under measurements saturation

To evaluate the impact of measurement saturation on SCI recovery, we randomly sampled mask values $D_{ij} \stackrel{\text{iid}}{\sim} \text{Bern}(p)$, incrementally varying p from 0.1 to 0.9 in steps of 0.1. The simulation results, presented in Fig. 3, were obtained using Algorithm 1. The results demonstrate that to minimize the upper bound on the reconstruction error—and thereby optimize performance—the value of p should remain below 0.5, as stated in Corollary 3.2.

Additionally, the results reveal that as the saturation level increases, the optimal value of p decreases. This observation also aligns with the theoretical predictions in Corollary 3.2, further validating the derived bounds and their implications for practical system design.

A closer examination of specific datasets, such as Drop, Crash, and Traffic, reveals that these datasets exhibit higher expected number of saturated measurements, as shown in Fig. 2. This increased susceptibility to saturation corresponds to a greater degradation in reconstruction quality, as evidenced by the comparison between Fig. 2 and Fig. 3. Consequently, these datasets stand to benefit considerably from mask optimization, underscoring the importance of tailoring mask distributions to the properties of specific data and imaging scenarios.

These results highlight the interplay between the saturation threshold, mask distribution, and data properties, emphasizing the need for careful design of masks to mitigate saturation effects and enhance SCI recovery performance.

6 Conclusion

In this paper, we analyzed the performance of SCI systems under measurement saturation and examined the role of binary mask optimization in mitigating its effects. Our theoretical insights show that binary masks with a Bernoulli distribution perform optimally when the probability of 1s (p) is less than 0.5, with further reductions needed as saturation levels increase. Simulations on benchmark datasets confirm the impact of optimizing masks on reconstruction quality and robustness, highlighting the critical link between mask parameters and recovery performance in saturated scenarios.

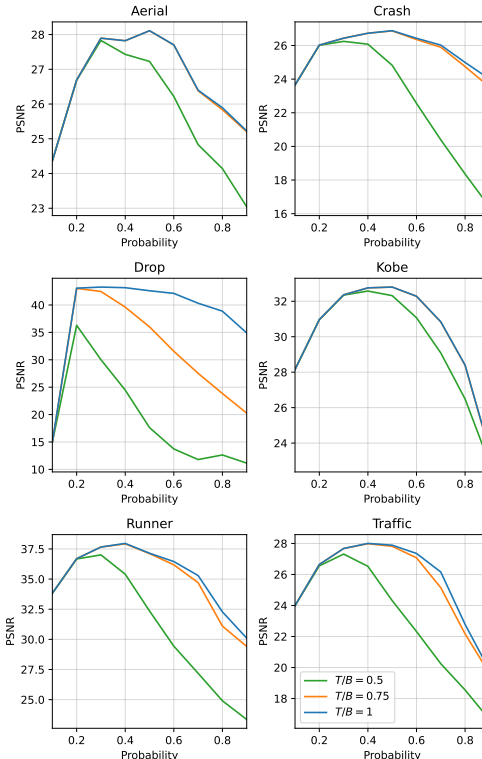


Figure 3: PSNR of $\|\mathbf{x} - \hat{\mathbf{x}}\|$ under different mask generated from $\text{Bern}(p)$ of different **saturation** level T .

References

- [1] M. E Gehm, R. John, D. J Brady, R. M Willett, and T. J Schulz. Single-shot compressive spectral imaging with a dual-disperser architecture. *Opt. Exp.*, 15(21):14013–14027, 2007.
- [2] Ashwin Wagadarikar, Renu John, Rebecca Willett, and David Brady. Single disperser design for coded aperture snapshot spectral imaging. *App. Opt.*, 47(10):B44–B51, 2008.
- [3] P. Llull, X. Liao, X. Yuan, J. Yang, D. Kittle, L. Carin, G. Sapiro, and D. J. Brady. Coded aperture compressive temporal imaging. *Opt. Exp.*, 21(9):10526–10545, 2013.
- [4] M. Qiao, Y. Sun, X. Liu, X. Yuan, and P. Wilford. Snapshot optical coherence tomography. In *Dig. Hol. and Three-Dim. Ima.*, pages W4B–3. Optica Publishing Group, 2019.
- [5] M. Iliadis, L. Spinoulas, and A. K. Katsaggelos. Deepbinarymask: Learning a binary mask for video compressive sensing. *Dig. Sig. Proc.*, 96:102591, 2020.
- [6] X. Zhang, Y. Zhang, R. Xiong, Q. Sun, and J. Zhang. Herosnet: Hyperspectral explicable reconstruction and optimal sampling deep network for snapshot compressive imaging. In *Proceedings of the IEEE/CVF conference on computer vision and pattern recognition (CVPR)*, pages 17532–17541, June 2022.
- [7] M. Zhao and S. Jalali. Theoretical analysis of binary masks in snapshot compressive imaging systems. In *2023 59th Annual Allerton Conf. on Comm., Cont., and Comp. (Allerton)*, pages 1–8. IEEE, 2023.
- [8] Mengyu Zhao, Xi Chen, Xin Yuan, and Shirin Jalali. Untrained neural nets for snapshot compressive imaging: Theory and algorithms. In *The Thirty-eighth Annual Conference on Neural Information Processing Systems*, 2024.
- [9] A. Wagadarikar, N. Pitsianis, X. Sun, and D. Brady. Video rate spectral imaging using a coded aperture snapshot spectral imager. *Opt. Exp.*, 17(8):6368–6388, Apr. 2009.
- [10] S. Jalali and A. Maleki. From compression to compressed sensing. *Appl. Comp. Harmonic Anal. (ACHA)*, 40(2):352–385, 2016.
- [11] S. Jalali and X. Yuan. Snapshot compressed sensing: Performance bounds and algorithms. *IEEE Trans. Inform. Theory*, 65(12):8005–8024, 2019.
- [12] M. Zhao and S. Jalali. Theoretical characterization of effect of masks in snapshot compressive imaging, 2025.
- [13] Jason N. Laska, Petros T. Boufounos, Mark A. Davenport, and Richard G. Baraniuk. Democracy in action: Quantization, saturation, and compressive sensing. *Applied and Computational Harmonic Analysis*, 31(3):429–443, 2011.
- [14] Simon Foucart and Jiangyuan Li. Sparse recovery from inaccurate saturated measurements. *Acta Applicandae Mathematicae*, 158(1):49–66, 2018.
- [15] Shuvayan Banerjee, Sudhansh Peddabomma, Radhendushka Srivastava, and Ajit Rajwade. A likelihood based method for compressive signal recovery under gaussian and saturation noise. *Signal Processing*, 217:109349, 2024.
- [16] P. Wang, L. Wang, and X. Yuan. Deep optics for video snapshot compressive imaging. In *Proceedings of the IEEE/CVF International Conference on Computer Vision (ICCV)*, pages 10646–10656, October 2023.
- [17] Bo Zhang, Xin Yuan, Chao Deng, Zhihong Zhang, Jinli Suo, and Qionghai Dai. End-to-end snapshot compressed super-resolution imaging with deep optics. *Optica*, 9, Apr 2022.

- [18] Christopher A. Metzler, Hayato Ikoma, Yifan Peng, and Gordon Wetzstein. Deep optics for single-shot high-dynamic-range imaging. In *Proceedings of the IEEE/CVF Conference on Computer Vision and Pattern Recognition (CVPR)*, June 2020.
- [19] Julien N. P. Martel, Lorenz K. Müller, Stephen J. Carey, Piotr Dudek, and Gordon Wetzstein. Neural sensors: Learning pixel exposures for hdr imaging and video compressive sensing with programmable sensors. *IEEE Transactions on Pattern Analysis and Machine Intelligence*, 42(7):1642–1653, 2020.
- [20] Nelson Diaz, Carlos Hinojosa, and Henry Arguello. Adaptive grayscale compressive spectral imaging using optimal blue noise coding patterns. *Optics and Laser Technology*, 2019.
- [21] Hao Zhang, Qing Ye, Ke Sun, Yangliang Li, Yunlong Wu, Haiping Xu, and Haoqi Luo. Anti-laser interference methods for compressive spectral imaging based on grayscale coded aperture. *Opt. Continuum*, 3, Jan 2024.
- [22] X. Yuan, Y. Liu, J. Suo, F. Durand, and Q. Dai. Plug-and-play algorithms for video snapshot compressive imaging. *IEEE Trans. Pattern Anal. Mach. Intell.*, 44(10):7093–7111, 2021.
- [23] X. Yuan. Generalized alternating projection based total variation minimization for compressive sensing. In *IEEE Int. Conf. on Image Proc. (ICIP)*, pages 2539–2543. IEEE, 2016.